Mesocell Study Area Snow Distributions for the Cold Land Processes Experiment (CLPX)

GLEN E. LISTON AND CHRISTOPHER A. HIEMSTRA

Cooperative Institute for Research in the Atmosphere, Colorado State University, Fort Collins, Colorado

KELLY ELDER

Rocky Mountain Research Station, USDA Forest Service, Fort Collins, Colorado

DONALD W. CLINE

NOAA/National Operational Hydrologic Remote Sensing Center, Chanhassen, Minnesota

ABSTRACT

The Cold Land Processes Experiment (CLPX) had a goal of describing snow-related features over a wide range of spatial and temporal scales. This required linking disparate snow tools and datasets into one coherent, integrated package. Simulating realistic high-resolution snow distributions and features requires a snow-evolution modeling system (SnowModel) that can distribute meteorological forcings, simulate snowpack accumulation and ablation processes, and assimilate snow-related observations. A SnowModel was developed and used to simulate winter snow accumulation across three 30 km × 30 km domains, enveloping the CLPX mesocell study areas (MSAs) in Colorado. The three MSAs have distinct topography, vegetation, meteorological, and snow characteristics. Simulations were performed using a 30-m grid increment and spanned the snow accumulation season (1 October 2002–1 April 2003). Meteorological forcing was provided by 27 meteorological stations and 75 atmospheric analyses grid points, distributed using a meteorological model (MicroMet). The simulations included a data assimilation model (SnowAssim) that adjusted simulated snow water equivalent (SWE) toward ground-based and airborne SWE observations. The observations consisted of SWE over three 1 km × 1 km intensive study areas (ISAs) for each MSA and a collection of 117 airborne gamma observations, each integrating area 10 km long by 300 m wide. Simulated SWE distributions displayed considerably more spatial heterogeneity than the observations alone, and the simulated distribution patterns closely fit the current understanding of snow evolution processes and observed snow depths. This is the result of the MicroMet/SnowModel's relatively finescale representations of orographic precipitation, elevation-dependant snowmelt, wind redistribution, and snow–vegetation interactions.

1. Introduction

Snow is an integral component of Earth's atmospheric, hydrologic, and ecologic systems. In many high-latitude and mountainous regions of the world, most of the annual precipitation falls as snow (e.g., Serreze et al. 1999). Of the various features that influence Earth's surface radiation balance, the location and du-ration of snow cover comprise two of the most important seasonal variables. In the Northern Hemisphere, the mean monthly land area covered by snow ranges from 5%–45% during the annual cycle (Robinson et al. 1993), making snow cover the most rapidly varying large-scale surface feature on earth. Snow's high albedo has a considerable influence on air temperatures and atmospheric circulation patterns (Ellis and Leathers 1999; Cohen and Entekhabi 2001). At finer scales, snow cover influences atmospheric and ground temperatures by moderating the conductive, sensible, and latent energy transfers among the atmosphere, snow cover, and ground (Liston 1995; Hinzman et al. 1998; Nelson et al.

Corresponding author address: Dr. Glen E. Liston, Cooperative Institute for Research in the Atmosphere, Colorado State University, Fort Collins, CO 80523-1375.
E-mail: liston@cira.colostate.edu

1998). Snow's low thermal conductivity insulates the soil from low winter air temperatures, leaving soils much warmer than they would be otherwise, and leading to lower nighttime air temperatures (Taras et al. 2002; Zhang et al. 2003). Snow cover affects soil–moisture conditions, runoff, and active-layer characteristics (Kane et al. 1991; Hinzman et al. 1996; Marsh 1999), and the spatial distribution of snow can influence spring snowmelt runoff timing, magnitude, and spatial variability (Luce et al. 1998).

In the Rocky Mountains, snow cover and depth patterns influence growing season length and plant distributions (Billings 1973; Fagre et al. 2003). Snow distributions affect atmospheric chemical inputs (Williams et al. 2002), ensuing meltwater distribution (Billings and Bliss 1959), mineral weathering (Benedict 1993), soil properties and development (Seastedt 2001), and decomposition and mineralization (Brooks et al. 1999). And finally, snow distributions play a critical role by acting as a freshwater reservoir, producing runoff for agricultural, domestic, industrial, and other uses. This snowmelt is particularly crucial for populations living in midlatitude arid regions, such as the southwestern United States. Snow-covered mountainous terrain in the headwaters of these arid regions can contribute 50%–80% of the annual downstream water supply (Wahl 1992).

In light of the role snow cover plays in influencing energy and moisture cycles within land, atmospheric, hydrologic, and ecologic systems, it is essential that models used to describe these systems include snow-related processes. Key snow distribution and evolution features include the considerable spatial and temporal variability that characterize snow accumulation and ablation processes. These variations are controlled by a combination of spatially and temporally variable atmospheric forcing conditions and how those forcings interact with relatively static local topography and vegetation distributions. Collectively, interactions among meteorology, topography, and vegetation produce snow covers that can have considerable spatial variability and can change significantly over time (e.g., Elder et al. 1991; Blöschl 1999; Balk and Elder 2000; Liston and Sturm 2002; Liston et al. 2002; Pomeroy et al. 2003; Essery and Pomeroy 2004; Gelfan et al. 2004; Hiemstra et al. 2006a).

The National Aeronautics and Space Administration (NASA) conducted the Cold Land Processes Field Experiment (CLPX) in Colorado during the winters of 2002 and 2003 (Elder et al. 2008a) to improve our understanding of, and our ability to describe with remote sensing and numerical models, the spatial distribution and temporal evolution of seasonal snow found within
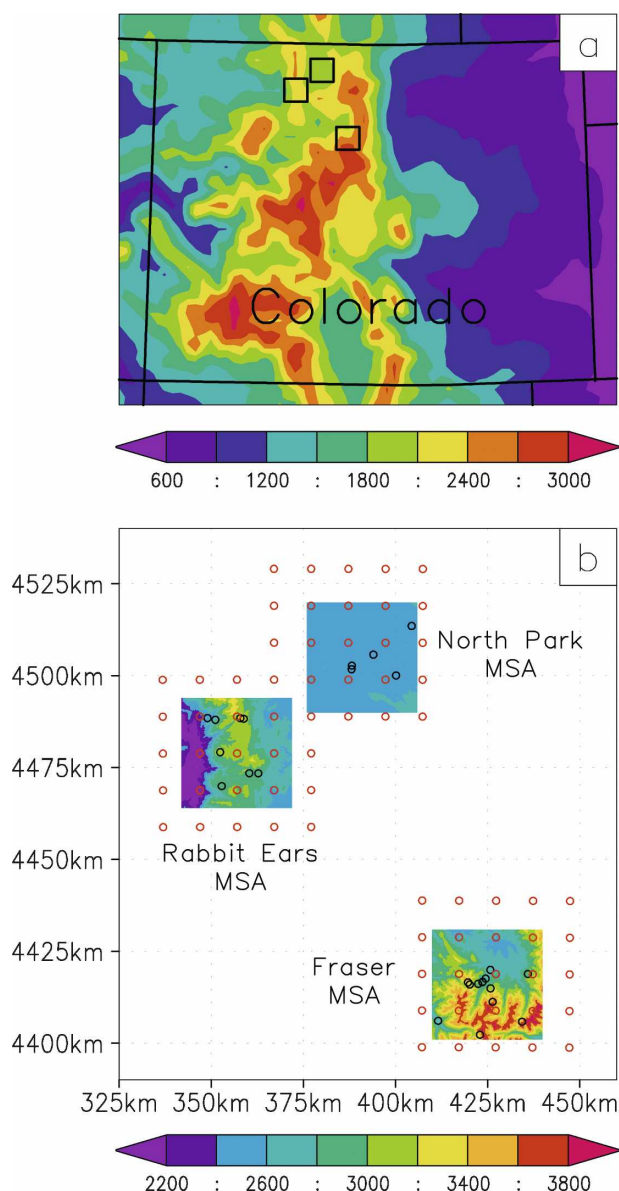

FIG. 1. (a) Locations of the three CLPX MSAs (shown by the small open squares in north-central Colorado) and the topography (m) of the surrounding area. (b) Details of the Fraser, North Park, and Rabbit Ears MSAs, showing the topography (m) in each 30 km × 30 km MSA simulation domain, the meteorological stations (black circles), and the LAPS atmospheric analysis model grid cells (red circles) used to provide the atmospheric forcing for the snow simulations. The coordinates in (b) are UTM Zone 13, Easting (km), and Northing (km).

cold regions and seasons. The CLPX experimental design included a collection of nested study areas, covering five different spatial scales. The middle-scale areas were called mesocell study areas (MSAs) and covered three 25 km × 25 km areas in north-central Colorado (Fig. 1). Each MSA was chosen because it represented

a distinct cold region physiographic regime, as defined by the area's topography, forest cover, meteorology, and snow characteristics. Nested within each of these MSAs were three 1 km × 1 km intensive study areas (ISAs). Snow-related observations for the ISAs included ground-based snow depth and density measurements (Elder et al. 2008a). Snow observations for the MSAs included airborne gamma radiation surveys (for snow water content), conducted along discrete flight lines over portions of each MSA (Cline et al. 2008).

In this paper, a snow-evolution modeling system (SnowModel; Liston and Elder 2006a) was used to simulate winter snow accumulation during the 2002/03 fall, winter, and early spring, for each of the three CLPX MSAs. Atmospheric forcings for the simulations were distributed using a meteorological model (MicroMet; Liston and Elder 2006b). To produce snow distributions consistent with CLPX snow observations, SnowModel assimilated available ISA and MSA snow measurements using the snow data assimilation (SnowAssim) submodel (Liston and Hiemstra 2008). The resulting datasets include daily (from fall to spring) snow water equivalent (SWE) distributions for each of the three MSAs at 30-m resolution. Because the data assimilation scheme constrains the model simulation to closely match the observations when and where they occur, simulated SWE distributions closely match coincident observational datasets and, because of the iterative nature of the method, they also represent temporally continuous and realistic distributions throughout the snow accumulation season. Thus, the resulting datasets are available for use in applications such as: comparing remote sensing datasets, providing subgrid snow distributions for relatively large-scale atmospheric and terrestrial modeling applications, defining subgrid snow distribution for remote sensing products such as the 25 km × 25 km Advanced Microwave Scanning Radiometer for Earth Observing System (AMSR-E) SWE datasets, and hydrologic applications such as snowmelt runoff studies.

2. Model description

SnowModel (Liston and Elder 2006a) is a spatially distributed snow-evolution modeling system, designed for application in all landscapes, climates, and conditions where snow occurs. It is an aggregation of the following three submodels: EnBal (Liston 1995; Liston et al. 2000) calculates surface energy exchanges, SnowPack (Liston and Hall 1995) simulates snow depth and water-equivalent evolution, and SnowTran-3D (Liston and Sturm 1998; Liston et al. 2007) accounts for snow redistribution by wind.

SnowModel is designed to run on grid increments of 1–200 m and temporal increments of 10 min–1 day. It can be applied using much larger grid increments, if the inherent loss in high-resolution (subgrid) information (Liston 2004) is acceptable. Simulated processes include an accumulation from snow precipitation; blowing-snow redistribution and sublimation; interception, unloading, and sublimation within forest canopies; snow density evolution; and snowpack ripening and melt. SnowModel incorporates first-order physics, required to simulate snow evolution within each of the global snow classes (i.e., ice, tundra, taiga, alpine/mountain, prairie, maritime, and ephemeral) defined by Sturm et al. (1995). An attractive feature of the distributed SnowModel is that, for example, it can blow and drift snow in an alpine area of the simulation domain while simultaneously melting valley snow. Required SnowModel inputs include temporally varying fields of precipitation, wind speed and direction, air temperature, and relative humidity, obtained from meteorological stations and/or an atmospheric model located within or near the simulation domain, and spatially distributed, invariant fields of topography and vegetation type.

Meteorological forcings required by SnowModel are provided by MicroMet (Liston and Elder 2006b), a quasiphysically based high-resolution (e.g., 1 m–1 km horizontal grid increment) meteorological distribution model. MicroMet is a data assimilation and interpolation model that uses meteorological station datasets and/or gridded atmospheric model, or analyses datasets. MicroMet minimally requires screen-height air temperature, relative humidity, wind speed and direction, and precipitation data. The model uses known relationships between meteorological variables and the surrounding landscape (primarily topography) to distribute those variables over any given landscape in physically plausible and computationally efficient ways. MicroMet performs two kinds of adjustments to the meteorological data: 1) all available data, at a given time, are spatially interpolated over the domain; and 2) physically based submodels are applied to each MicroMet variable to quantify topographic and elevation effects at any given point in space and time. Station interpolations (horizontal) to a regular grid are done using a Barnes objective analysis scheme (Barnes 1964, 1973; Koch et al. 1983). The Barnes scheme applies a Gaussian distance-dependent weighting function, in which the weight that a station contributes to the overall value of the grid point decreases with increasing distance from the observation. Interpolation weights are objectively determined as a function of data spacing and distribution. At each time step, MicroMet gener-

ates distributions of air temperature, relative humidity, wind speed and direction, incoming solar and longwave radiation, surface pressure, and precipitation, and makes them accessible to SnowModel.

SnowModel also includes SnowAssim (Liston and Hiemstra 2008). The data assimilation scheme is consistent with optimal interpolation approaches in which the differences between observed and modeled snow values constrain modeled outputs. The calculated corrections are applied backward in time to create improved fields prior to the assimilated observations. Thus, one of the values of this scheme is improved simulation of snow-related distributions throughout the entire snow season, even when observations are only available sporadically or late in the accumulation and/ or ablation periods. Because of this, the technique is particularly applicable to reanalysis applications, such as those presented herein. The methodology includes the ability to stratify the assimilation into regions where either the observations and/or model has unique error properties, such as the differences between forested and nonforested snow environments.

3. Model simulations

a. Model configuration and simulation domains

Winter snow evolution was simulated from 1 October 2002 to 1 April 2003 for each of the three CLPX MSAs defined by Elder et al. (2008a): Fraser, North Park, and Rabbit Ears in north-central Colorado (Fig. 1). For the mountainous terrain of Fraser and Rabbit Ears, this simulation period spans the snow accumulation season, from initial snow accumulation in the fall to beginning ablation in the spring. North Park also accumulates snow during this period, but because it is at a lower elevation and in the precipitation shadow of the surrounding mountains, snow depths are shallower, and the snowpack is short lived and possibly intermittent. The spatial domain of each simulation covered a 30 km × 30 km area centered over each 25 km × 25 km CLPX MSA; we defined these larger areas to ensure that our model simulations and outputs always included MSA-related observations. In the discussions that follow, MSA refers to the 30 km × 30 km simulation areas. Model simulations were performed using a 30-m horizontal grid increment over each MSA (1001 grid cells in each of the x and y directions, or ~1 000 000 grid cells). This 30-m grid increment strikes a balance between available computer resources and the need to accurately represent the driving snow-distribution processes found within each of the MSAs. In addition, the simulations used a 1-day time increment to keep computational requirements within acceptable limits. Al-

though this may not be acceptable during the ablation season when diurnal melt cycles are often important to resolve, it is expected to have minimal influence during the accumulation season. Topographical data (30-m horizontal and 1-m vertical resolution) for the MSA domains were obtained from the U.S. Geological Survey National Elevation Dataset. Vegetation data of identical horizontal resolution were obtained from the 1992 National Land Cover Data (Vogelmann et al. 2001) and reclassified to match SnowModel's defined vegetation classes (Liston and Elder 2006a).

The Fraser MSA is characterized by complex, mountainous topography, with a large north–south topographic gradient (Fig. 2a). The southern half of the MSA contains the highest and most rugged peaks, whereas the northern half has more gentle mountain slopes and broad valleys. It has minimum, maximum, and mean elevations of 2489, 4052, and 3081 m, respectively. Vegetation (Fig. 2b) at the relatively low elevations to the north consists of irrigated meadows and lodgepole pine (*Pinus contorta* var. *latifolia*) forests. The highest elevation areas in the south are predominantly alpine tundra or bare rock. The montane areas in between are dominated by coniferous forests, generally with spruce-fir (*Picea engelmannii* and *Abies lasiocarpa*) on the wetter north-facing slopes and lodgepole pine on the drier south-facing slopes. The Fraser MSA typically has moderate-to-deep snow covers that increase with elevation.

The North Park MSA lies within the center of a broad high-elevation parkland, approximately 40 km in diameter. Compared with the Fraser MSA, North Park is relatively flat (Fig. 3a). It has minimum, maximum, and mean elevations of 2399, 2804, and 2502 m, respectively. Vegetation in the area is mostly sagebrush (*Artemisia tridentata* var. *vaseyana*) shrubland, with meadows in the wetter areas near rivers and streams (Fig. 3b). Relatively little snow accumulates within North Park because of the precipitation shadows caused by surrounding mountain ranges.

The Rabbit Ears MSA includes the flat uplands of Rabbit Ears Pass across the Park Range of north-central Colorado (Fig. 4a). The uplands are flanked to the east and west by steep valleys and the relatively flat terrain of the river valleys and basins below. It has minimum, maximum, and mean elevations of 2025, 3330, and 2678 m, respectively. The upland portion of the MSA contains low-to-moderate topographic relief that extends north–south through the middle of the MSA. In the upland areas, forest cover consists of spruce fir, lodgepole pine, and aspen (*Populus tremuloides*), interspersed with broad glades and grassy meadows (Fig. 4b). Vegetation in the lower elevations
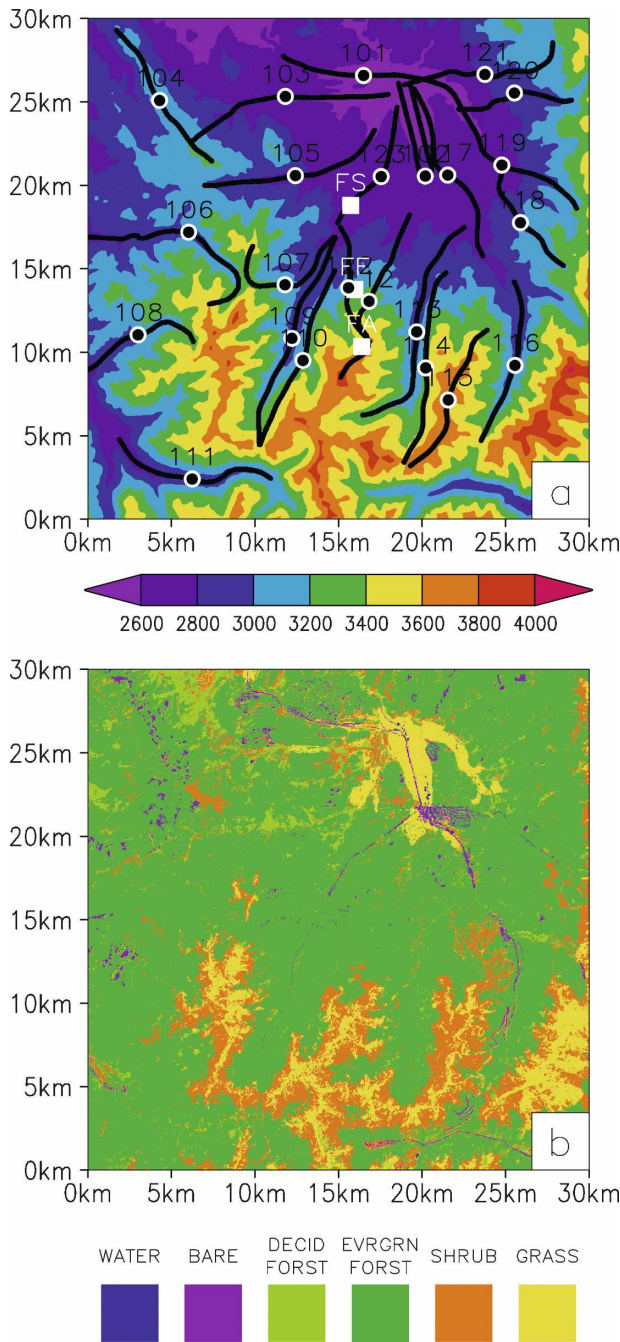
FIG. 2. Fraser MSA (a) topography (m), and (b) vegetation. Also shown in (a) are the intensive study areas (white squares: FS = Fraser, St. Louis Creek; FF = Fraser, Fool Creek; FA = Fraser, Alpine), and the GAMMA flight lines (black lines with black and white markers and ID numbers in the center of each line).

FIG. 3. Same as Fig. 2, but for North Park MSA, with NP = North Park, Potter Creek; NI = North Park, Illinois River; and NM = North Park, Michigan River. For clarity, the flight lines alternate gray and black, do not include black and white markers, and only every other line is labeled with an ID number.

to the east and west consists of shrublands and pastures. The upland area receives heavy snowfall during the winter and spring, often developing the deepest snowpacks in Colorado (Doesken and Judson 1996).
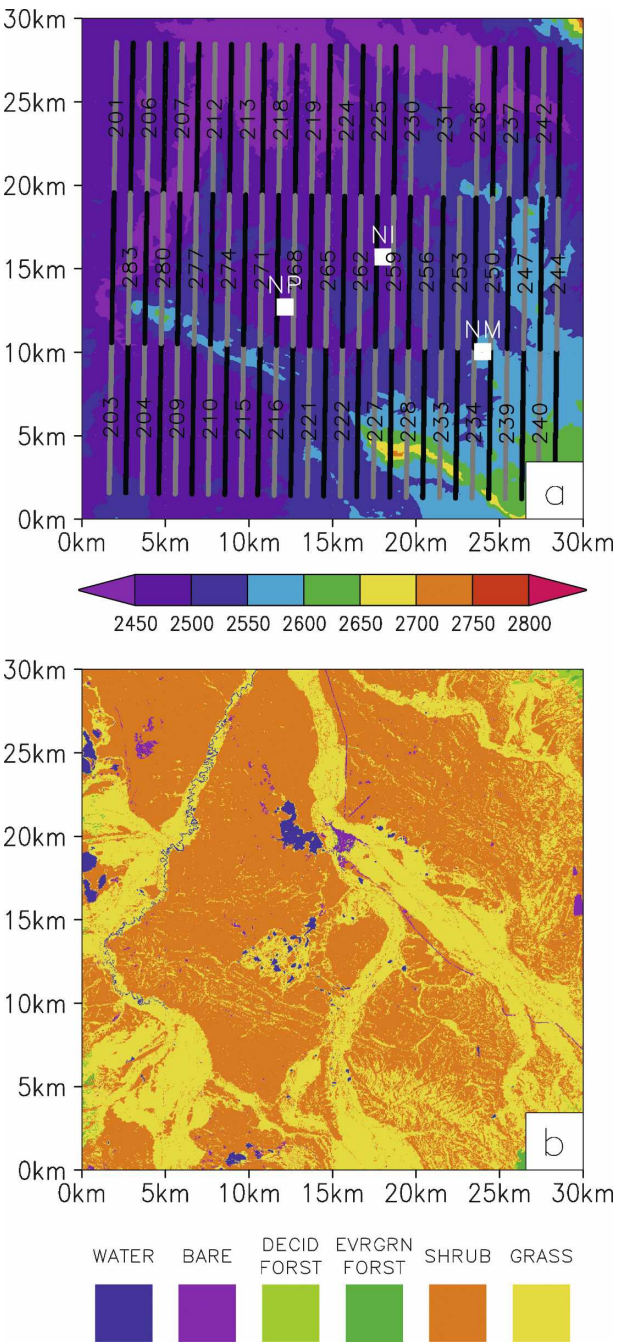
b. Snow observations

The data assimilation incorporated two kinds of observational datasets: 1) ground-based snow depth and density observations collected at each of the nine ISAs
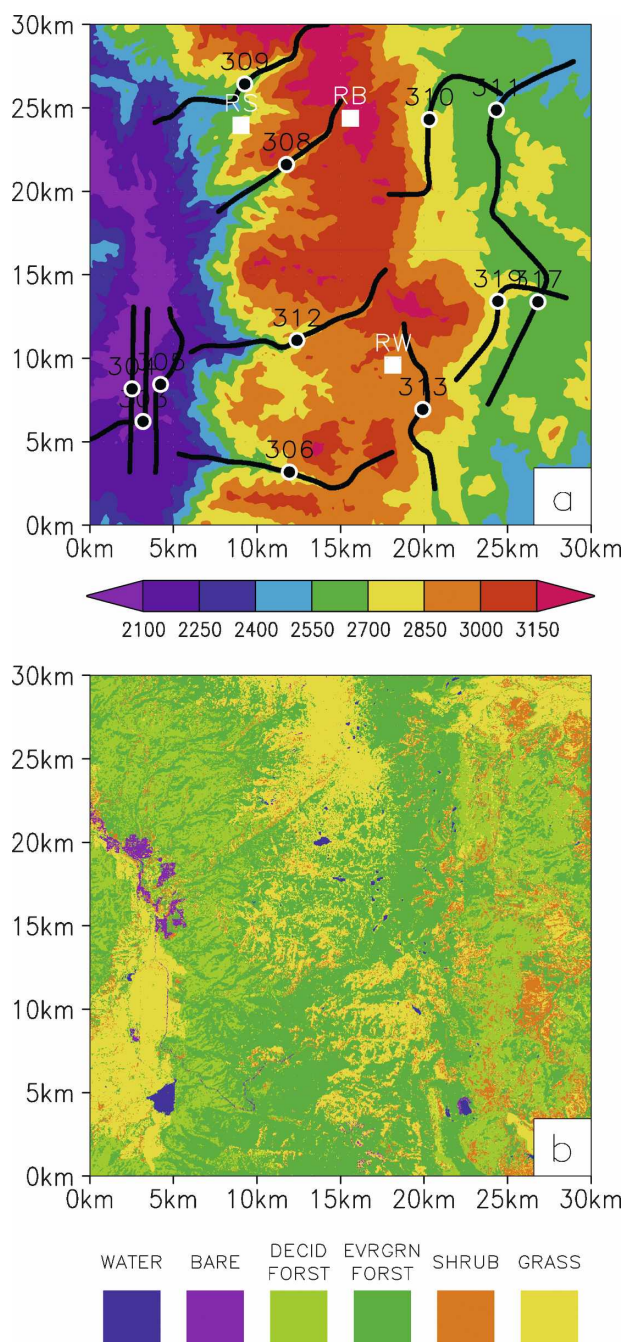
FIG. 4. Same as Fig. 2, but for Rabbit Ears MSA, with RS = Rabbit Ears, Spring Creek; RB = Rabbit Ears, Buffalo Pass; and RW = Rabbit Ears, Walton Creek.

(Elder et al. 2008a), and 2) airborne measurements of gamma radiation emitted from earth and converted to a measure of snowpack SWE (Cline et al. 2008). CLPX included four intensive observing periods (IOPs) during the winters of 2001–02 and 2002–03. These focused on two characteristic periods each year: 1) midwinter

(19–25 February; IOP1 and IOP3), when frozen conditions and relatively dry snow conditions are typical; and 2) early spring (25 March–1 April; IOP2 and IOP4), when transitional (e.g., frozen and thawed) conditions and relatively wet snow conditions are prevalent. The simulations presented herein focus on winter 2002–03 and IOP3 and IOP4.

CLPX ground-based snow depth and density observations from IOP3 and IOP4 were used to estimate area-averaged SWE for each of the nine CLPX ISAs. All snow depth measurements were averaged over each ISA, including zero-depth values resulting from observations made at snow-free observation points. With 684 potential depth observations randomly distributed over each 1-km^2 ISA [see Elder et al. (2008a) for a detailed description of the measurement protocols], this mean depth value was assumed to serve as an effective surrogate for mean ISA snow depth and includes the effective snow-covered area. Because of survey conditions and available personnel, depth values collected in each ISA ranged from 455 to 684, with the majority close to 684 (15 of the 18 cases had more than 625 points). Mean density was calculated using all available snow pit densities for each ISA and IOP. The number of snow pit density profiles varied from 3 to 16 between sites as a result of weather constraints, with the majority of ISAs having close to 16 (14 of the 18 cases had 16 density profiles). The mean SWE for each ISA and for IOP3 and IOP4 was calculated as the product of mean depth and percent (snow/water) mean density (Table 1).

The gamma SWE observations are derived from measurements of natural terrestrial gamma radiation emitted from potassium (^{40}K), uranium (^{238}U), and thorium (^{232}Th) radioisotopes in the upper 20 cm of soil. As part of the measurement program, the radiation is measured from an aircraft flying 150 m above the ground. Terrestrial gamma rays are attenuated by the atomic cross section of intervening mass (e.g., water in any phase, vegetation, and air) between the soil and the aircraft. The measurement of the attenuation (i.e., the difference between measurements over dry soil and measurements over moist soil or snow) has been found to be a reliable basis for soil moisture and SWE measurements (Jones and Carroll 1983). Using the Gamma Radiation Detection System (GAMMA), this technique has been used operationally by the National Weather Service (NWS) since 1979 to measure mean areal SWE and soil moisture along aircraft flight lines (Peck et al. 1980; Jones and Carroll 1983; Carroll 1987). The instrument and aircraft used for CLPX were operated by the NWS National Operational Hydrologic Remote Sensing Center (NOHRSC).

TABLE 1. Area-averaged snow depth and density, and SWE for the CLPX ISAs during IOP3 (20–25 Feb 2003) and IOP4 (26–31 Mar 2003).

	IOP 3			IOP 4		
	Mean depth (cm)	Mean density (kg m^{-3})	Mean SWE (cm)	Mean depth (cm)	Mean density (kg m^{-3})	Mean SWE (cm)
Fraser ISA						
St. Louis Creek	58.3	228.5	13.3	97.5	285.4	27.8
Fool Creek	93.6	242.1	22.7	176.3	251	44.3
Alpine	77.8	244.7	19.0	144.9	270.1	39.1
North Park ISA						
Illinois River	6.8	223.8	1.5	5.2	164.8	0.9
Michigan River	9.3	182.3	1.7	6.6	178.4	1.2
Potter Creek	5.3	202.7	1.1	3.5	149.3	0.5
Rabbit Ears ISA						
Buffalo Pass	275.3	258.7	71.2	322.5	340.3	109.8
Spring Creek	204.4	254.1	51.9	209.3	321.1	67.2
Walton Creek	197.1	255.9	50.4	203.1	329.3	66.9

The CLPX GAMMA datasets used in model simulations include SWE observations collected in series of flight lines within each of the three MSAs (Figs. 2a–4a). Initial background terrestrial gamma radiation measurements were collected under relatively dry soil conditions, with no snow cover present in September 2001 for 23 flight lines in the Fraser MSA, 84 flight lines in the North Park MSA, and 22 flight lines in the Rabbit Ears MSA. Coincident ground observations of gravimetric soil moisture were collected to estimate the mean soil moisture along each flight line. This was used to calibrate the background radiation measurements, accounting for the attenuation effects of existing soil moisture. The absorption and reradiation of gamma radiation by intervening vegetation mass was also accounted for in the snow-free calibration gamma observations. Subsequent measurements of terrestrial gamma radiation over the flight lines during the experiment were used to determine the attenuation of the radiation signal solely because of the intervening water mass in the snow and soil. SWE was determined by estimating the proportion of attenuation resulting from soil moisture. In this case, the subnivean soil moisture was assumed to be identical to the background calibration. If this assumption is incorrect, for example, a 5% gravimetric soil moisture increase (decrease) corresponds to an approximately 0.8-cm SWE increase (decrease; T. R. Carroll and D. W. Cline 2007, personal communication), because the GAMMA system is measuring changes in both soil moisture and SWE. Depending on soil field holding capacities, the total possible error is a few centimeters. This potential error varies with overall snow depth and snowpack characteristics. Although deeper snowpacks can be affected, the possible errors are relatively small compared with

deeper SWE. In contrast, the relative error for shallow snowpacks can approach the actual SWE. Furthermore, the likelihood that this assumption is incorrect increases in areas with shallow snowpacks, where soil moisture can change rapidly throughout the winter as snow arrives and melts and the resulting soil moisture evaporates.

The North Park GAMMA flight plan consisted of 28 parallel series of three 9-km flight lines, with each series spaced 1 km apart (Fig. 3a). Together, these 84 SWE samples provide coverage of approximately 30% of the MSA area. A comparison of average SWE for the three North Park ISAs during IOP3 (1.43 cm) and IOP4 (0.85 cm; Table 1), with North Park GAMMA observations for IOP3 (4.62 cm) and IOP4 (5.40 cm; Cline et al. 2008), suggested that considerable errors may exist in the GAMMA values and assumptions over North Park's shallow snow. To account for soil moisture changes that occurred between the fall 2001 gamma-ray background calibration flight and the IOP3 and IOP4 flights, soil moistures measured during IOP3 and IOP4 were used to adjust the original GAMMA values. For IOP3, 84 gravimetric soil moisture observations yielded minimum, maximum, mean, and standard deviations of 10%, 85%, 29%, and 18%, respectively (Elder et al. 2008a). Assuming that the soil moisture for each flight line was estimated with 0% error during the fall background calibration, the difference between the 29% moisture during IOP3 and the nominal 15% value used during the calibration yielded [(29–15)*0.8/5], a reduction of 2.2 cm SWE for each IOP3 flight line. For IOP4, 37 gravimetric soil moisture observations yielded minimum, maximum, mean, and standard deviations of 6%, 31%, 15%, and 5%, respectively. Therefore, because the mean observed soil moisture equaled the nominal

TABLE 2. Fraser MSA ground-based observations from ISAs and GAMMA flights (ID numbers correspond to those given in Fig. 2a). Shown are the coordinates of the ISA and flight line centers and the mean SWE for the corresponding areas. Also included are the differences for the corresponding ISA and flight line areas (difference = modeled − observed). The IOP date for IOP3 is 19 Feb and 25 Mar 2003 for IOP 4.

Observation ID	Easting (m)	Northing (m)	IOP3 observed SWE (cm)	IOP3 difference SWE (cm)	IOP4 observed SWE (cm)	IOP4 difference SWE (cm)
St. Louis Creek ISA	425 753	4 419 809	13.3	0.0	27.8	−0.6
Fool Creek ISA	425 988	4 414 759	22.7	−3.6	44.2	−4.5
Alpine ISA	426 403	4 411 344	19.0	4.7	39.1	1.0
101	426 525	4 427 590	10.7	3.6	17.0	7.0
102	430 192	4 421 540	14.7	0.2	23.4	3.9
103	421 842	4 426 305	19.8	−1.1	30.5	−0.1
104	414 291	4 426 064	29.7	0.8	45.5	2.8
105	422 417	4 421 570	17.0	−0.6	26.7	2.1
106	416 040	4 418 174	16.3	4.3	25.9	8.4
107	421 804	4 415 038	22.1	−1.9	43.7	−5.7
108	413 004	4 412 025	16.5	2.1	27.9	3.9
109	422 233	4 411 826	15.0	−0.6	28.2	−0.1
110	422 878	4 410 521	17.0	−0.5	31.0	1.2
111	416 263	4 403 397	15.2	1.8	24.4	3.5
112	426 831	4 414 045	17.3	6.1	35.1	9.0
113	429 705	4 412 231	16.3	−3.4	29.2	−2.9
114	430 241	4 410 062	17.5	−3.1	34.8	−4.1
115	431 593	4 408 151	11.9	18.6	25.4	28.9
116	435 565	4 410 215	19.1	−5.7	31.5	−6.6
117	431 560	4 421 605	13.0	1.6	21.3	6.1
118	435 902	4 418 759	16.0	0.6	32.0	0.6
119	434 778	4 422 209	13.7	0.7	26.4	−0.6
120	435 549	4 426 543	13.0	0.7	24.1	0.9
121	433 757	4 427 624	13.0	−0.6	23.9	−1.2
122	425 616	4 414 845	18.5	−0.1	35.3	1.6
123	427 552	4 421 520	11.2	2.9	22.1	1.8

15% value used in the original SWE calculation, no adjustment was made to the IOP4 GAMMA observations. For IOP3 and IOP4, there was no discernable trend or spatial pattern to the observed soil moisture values (maps of the point values look nearly random), thus supporting our use of a block adjustment for the IOP3 GAMMA values. The adjusted IOP GAMMA values now averaged 2.32 cm for IOP3 and 5.40 cm for IOP4. These were still considerably different than those measured within the North Park ISAs (Table 1). Under the assumption that the ISA SWE values accurately represent SWE within the ISAs, and the average of these ISA values represents SWE values over the North Park MSA, we performed the following additional adjustment to the North Park GAMMA data: each North Park GAMMA value was multiplied by the ratio of the ISA average to the GAMMA average for each IOP. This effectively produced GAMMA values that averaged to equal the ISA mean, while still preserving the spatial variability contained within the uncorrected GAMMA observations.

The Fraser MSA had 23 flight lines (Fig. 2a) and the Rabbit Ears MSA had 22 flight lines (Fig. 4a). For these study sites, ground coverage by the flight lines was much less than North Park (Fig. 3a), as a result of terrain constraints on low-altitude flight. The lines generally followed valleys, ridges, and elevation contours. Soil moisture error was not an issue in the relatively deep Fraser and Rabbit Ears snowpacks. The GAMMA SWE data used in the model simulations, for IOP3 and IOP4, are listed in Tables 2–4, for Fraser, North Park, and Rabbit Ears, respectively.

c. Meteorological forcing

Meteorological data used in the model simulations take two primary forms: meteorological station data (Elder et al. 2008b) and atmospheric analysis data (Liston et al. 2008). A network of ground-based meteorological observing stations was deployed as part of CLPX (Elder et al. 2008b). The objective of measuring meteorological parameters was to quantify variability from local to regional scales within various snow environments and to provide forcing data for algorithm and model development and verification. Ten identical 12-m instrument towers were erected at CLPX study sites during summer 2002 (one reason why we do not

present simulations from the 2001–02 snow season is because these ISA meteorological towers were not yet installed). Nine towers were placed at or near the center of the nine ISAs, and one was installed near the headquarters building at the Fraser Experimental Forest. At each of these towers, air temperature, relative humidity, and wind speed and direction were measured from a cross arm mounted 10 m above the ground surface and used for the simulations presented herein (see Elder et al. 2008b for a complete list of the measured variables). In addition, a CLPX eddy covariance flux tower was installed in the North Park MSA, and 16 other meteorological stations were available from a variety of existing networks maintained by the Forest Service, the Natural Resource Conservation Service, Remote Automated Weather Stations (RAWS), and the Desert Research Institute (DRI). Table 5 provides a listing of the meteorological stations used and the associated variables. Station locations are also identified in Fig. 1b.

Atmospheric analysis data from the Local Analysis and Prediction System (LAPS; McGinley et al. 1991; Albers 1995; Albers et al. 1996; Birkenheuer 1999; Hiemstra et al. 2006b) were also used to provide meteorological forcing for the MSA simulations. During CLPX, LAPS was run by the National Oceanic and Atmospheric Administration's Earth System Research Laboratory (NOAA/ESRL) using a 10-km horizontal grid (125 × 105), with 21 isobaric vertical levels and hourly temporal resolution. The LAPS analysis domain covers Colorado, Wyoming, and parts of the surrounding states. These analyses incorporated a wide range of observational datasets, including: 1) surface observations from regional surface networks every 5 min–3 h, 2) hourly surface aviation observations, 3) Doppler radar volume scans every 6–10 min, 4) wind and temperature radio acoustic sounding system (RASS) profiles from the NOAA Demonstration Profiler Network every 6–60 min, 5) satellite visible data every 15–30 min, 6) multispectral image and sounding radiance data every 60 min, 7) global positioning system (GPS) total precipitable water vapor determined from signal delay, and 8) automated aircraft observations. The resulting LAPS outputs include spatially and temporally continuous atmospheric state variables over the analysis domain (Liston et al. 2008). Each 5 × 5 group of LAPS grid cells that covered a CLPX MSA was used in the MicroMet–SnowModel–SnowAssim simulations (Fig. 1b).

To prepare the meteorological station and LAPS datasets for the model simulations, the MicroMet preprocessor (Liston and Elder 2006b) was used to analyze and correct the original data. First, missing values were identified. Second, the preprocessor performed three quality assurance/quality control (QA/QC) data tests following Meek and Hatfield (1994). Test 1 checked for values outside acceptable ranges, test 2 looked for consecutive values that exceed acceptable increments, and test 3 found constant consecutive values with no observed change. Third, the preprocessor filled missing data with calculated values; this was done in a variety of ways, all designed to preserve diurnal cycles and other characteristics of the remaining data [see Liston and Elder (2006b) for additional details]. In addition, for stations located within or below forest canopies, wind speed and direction observations were assumed to be missing (Table 5); this allowed MicroMet to first simulate top-of-canopy wind fields and then calculate canopy-appropriate wind speed reductions and distributions.

To ensure consistent precipitation forcing among the three MSAs, all precipitation data were provided by LAPS analyses (Table 5). Because of the known limitations in the ability of relatively coarse-resolution atmospheric models to simulate true precipitation in mountainous terrain (see Hiemstra et al. 2006b; Liston and Elder 2006b), LAPS precipitation fields for each MSA were multiplied by an adjustment number, such that the MSA-average SnowModel data assimilation correction factor for the MSA averaged near unity for the two IOPs (these correction factors are discussed further in the next section). Resultant precipitation adjustment numbers were 9, 3, and 66, for the Fraser, North Park, and Rabbit Ears MSAs, respectively. The high value for Rabbit Ears is a result of the minimal precipitation data available for use in the LAPS assimilation; thus, LAPS defined low precipitation values and possibly the relatively high precipitation values found in this area. MicroMet identified which meteorological variables are available from the collection of possible meteorological stations and LAPS grid points and uses those to create the necessary distributions. After performing these preprocessing steps, MicroMet created the required daily spatial distributions of the meteorological variables for SnowModel.

4. Model results

The main model simulation results are presented in three four-panel figures, one for each MSA (Figs. 5–7 for Fraser, North Park, and Rabbit Ears, respectively). These panels represent the spatial distributions of the observed SWE, the data adjustments imposed by Snow-Assim, the model-simulated SWE, and the differences between the modeled and observed SWE. IOP3 results are not shown for Fraser and Rabbit Ears; the patterns

TABLE 3. North Park MSA ground-based observations from ISAs and GAMMA flights (ID numbers correspond to those given in Fig. 3a). Shown are the coordinates of the ISA and flight line centers and the mean SWE for the corresponding areas. Also included are the differences for the corresponding ISA and flight line areas (difference = modeled − observed). The IOP date for IOP3 is 21 Feb and 28 Mar 2003 for IOP4.

Observation ID	Easting (m)	Northing (m)	IOP3 observed SWE (cm)	IOP3 difference SWE (cm)	IOP4 observed SWE (cm)	IOP4 difference SWE (cm)
Illinois River ISA	394 004	4 505 710	1.5	−1.2	0.9	−0.9
Michigan River ISA	399 994	4 500 040	1.7	0.3	1.2	−1.1
Potter Creek ISA	388 153	4 502 710	1.1	−0.8	0.5	−0.5
201	378 005	4 514 075	2.7	−0.6	1.0	−0.6
202	377 857	4 505 094	1.9	−0.2	0.9	−0.6
203	377 709	4 496 103	0.9	−0.1	0.8	−0.5
204	379 689	4 496 070	0.6	0.4	0.7	−0.3
205	379 834	4 505 051	1.1	0.6	0.8	−0.2
206	379 980	4 514 043	2.2	0.4	1.0	−0.1
207	381 947	4 514 011	2.8	−0.3	0.9	−0.6
208	381 803	4 505 019	1.6	0.2	0.8	−0.3
209	381 660	4 496 039	0.9	−0.1	0.9	−0.5
210	383 632	4 496 008	1.2	−0.8	0.8	−0.5
211	383 772	4 504 988	1.4	0.2	0.7	−0.5
212	383 913	4 513 980	1.6	0.6	0.8	0.1
213	385 888	4 513 949	1.9	−0.3	0.7	−0.5
214	385 749	4 504 958	1.9	−0.6	0.8	−0.7
215	385 611	4 495 977	0.3	0.1	0.7	−0.2
216	387 583	4 495 947	0.8	−0.4	0.7	−0.4
217	387 718	4 504 928	1.7	−0.7	0.8	−0.7
218	387 863	4 513 919	1.7	−0.6	0.8	−0.7
219	389 830	4 513 901	1.6	−0.6	0.7	−0.6
220	389 696	4 504 909	0.8	−0.2	0.6	−0.6
221	389 562	4 495 917	0.9	−0.4	0.7	−0.6
222	391 533	4 495 877	1.6	−1.3	1.2	−1.1
223	391 665	4 504 880	1.1	−0.5	0.7	−0.7
224	391 796	4 513 872	1.4	−0.3	0.6	−0.5
225	393 762	4 513 832	2.2	−0.8	0.8	−0.8
226	393 634	4 504 852	1.6	−0.8	0.7	−0.7
227	393 505	4 495 860	1.1	−0.2	1.0	−0.9
228	395 485	4 495 832	0.8	0.1	0.9	−0.8
229	395 611	4 504 823	0.9	0.3	0.6	−0.6
230	395 737	4 513 815	1.4	0.5	0.7	−0.6
231	397 704	4 513 777	2.5	−0.3	0.8	−0.8
232	397 580	4 504 785	0.9	0.5	0.6	−0.6
233	397 464	4 495 804	1.1	−0.2	0.9	−0.9
234	399 427	4 495 778	1.4	−0.5	1.0	−1.0
235	399 549	4 504 769	1.9	0.1	1.1	−1.1
236	399 670	4 513 761	1.4	0.5	0.7	−0.7
237	401 645	4 513 723	—	—	0.8	−0.8
238	401 526	4 504 732	—	—	1.2	−1.2
239	401 398	4 495 751	—	—	1.4	−1.3
240	403 378	4 495 725	—	—	1.8	−1.3
241	403 495	4 504 706	—	—	1.2	0.5
242	403 612	4 513 708	—	—	1.1	−1.0
243	404 591	4 513 696	—	—	1.0	−1.0
244	404 475	4 504 693	—	—	1.3	0.8
245	404 368	4 495 701	—	—	2.1	−1.0
246	402 388	4 495 727	—	—	1.7	−1.7
247	402 506	4 504 719	—	—	1.3	−0.3
248	402 624	4 513 710	—	—	1.0	−1.0
249	400 658	4 513 736	—	—	0.9	−0.8
250	400 537	4 504 745	—	—	1.1	−1.0
251	400 417	4 495 753	—	—	1.0	−1.0
252	398 446	4 495 780	—	—	0.9	−0.9
253	398 568	4 504 771	—	—	0.8	−0.8

TABLE 3. (*Continued*)

Observation ID	Easting (m)	Northing (m)	IOP3 observed SWE (cm)	IOP3 difference SWE (cm)	IOP4 observed SWE (cm)	IOP4 difference SWE (cm)
254	—	—	—	—	—	—
255	—	—	—	—	—	—
256	396 591	4 504 799	—	—	0.6	−0.6
257	396 466	4 495 807	—	—	0.9	−0.9
258	394 495	4 495 835	—	—	1.0	−0.9
259	394 622	4 504 826	—	—	0.7	−0.7
260	394 750	4 513 818	—	—	0.8	−0.7
261	392 783	4 513 846	—	—	0.8	−0.7
262	392 653	4 504 855	—	—	0.7	−0.7
263	392 523	4 495 863	—	—	1.0	−1.0
264	390 544	4 495 892	—	—	0.8	−0.7
265	390 684	4 504 883	—	—	0.7	−0.7
266	390 817	4 513 886	—	—	1.1	−1.1
267	388 842	4 513 904	—	—	1.0	−0.7
268	388 707	4 504 913	—	—	0.6	−0.5
269	388 572	4 495 921	—	—	0.7	−0.4
270	386 601	4 495 951	—	—	0.6	−0.1
271	386 738	4 504 942	—	—	0.7	−0.5
272	386 875	4 513 934	—	—	0.5	−0.3
273	384 901	4 513 965	—	—	0.4	−0.3
274	384 761	4 504 973	—	—	0.6	−0.5
275	384 621	4 495 981	—	—	0.6	−0.2
276	382 650	4 496 012	—	—	0.6	−0.3
277	382 792	4 505 004	—	—	0.4	−0.1
278	382 934	4 514 007	—	—	0.5	0.0
279	380 968	4 514 027	—	—	0.8	−0.1
280	380 823	4 505 035	—	—	0.6	0.0
281	380 679	4 496 043	—	—	0.8	−0.4
282	378 699	4 496 075	—	—	0.6	−0.3
283	378 846	4 505 067	—	—	0.7	−0.2
284	378 993	4 514 059	—	—	0.6	0.0

are similar, but the SWE magnitudes are reduced because IOP3 was earlier in the snow accumulation season. North Park MSA SWE magnitudes were greater in IOP3 than IOP4 (Table 3); thus, Fig. 6 displays IOP3 data.

Figure 5 displays the results of the Fraser MSA simulation for IOP4. For reference, Fraser ISA and GAMMA observation masks were superimposed on Figs. 5a and 5d. The ISA and GAMMA SWE observations were interpolated to the simulation grid using MicroMet's Barnes spatial interpolation scheme (Fig. 5a). To perform this interpolation, the average SWE for each ISA and GAMMA flight line was defined to fall in the center of the ISA/flight line, and the resulting point values were interpolated over the domain. The relatively deep snow in the northwest corner of the domain is a result of the highest observed SWE value on Fraser flight line 104, located in that corner (Fig. 2a; Table 2). Flight lines 104 and 115 were the only Fraser GAMMA lines that followed ridges; all others occurred in valleys or relatively flat areas.

During model simulations, SnowModel performed an initial simulation over the entire period. The results of this simulation were compared against concurrent observations. Under the assumption that the differences between the model and the observations are largely the result of errors in the precipitation fields, a precipitation correction was calculated (Liston and Hiemstra 2008). Although this assumption is considered justified in light of the previous discussion of the LAPS precipitation fields used in the model simulations, it has not been made using a rigorous analyses of the precipitation errors and the errors associated with the other input fields. The imposed correction can be different for each interval between available observations. The precipitation correction factor distributions (Fig. 5b) were then used to scale the precipitation fields in the initial simulation, and this new precipitation forcing was used for a secondary and final simulation (Fig. 5c). The final SWE distribution displays relatively finescale structure related to orographic precipitation, low-elevation melt, wind redistribution (snow drifts above

TABLE 4. Rabbit Ears MSA ground-based observations from ISAs and GAMMA flights (ID numbers correspond to those given in Fig. 4a). Shown are the coordinates of the ISA and flight line centers and the SWE for the corresponding areas. Also included are the differences for the corresponding ISA and flight line areas (difference = modeled − observed). The IOP date for IOP3 is 24 Feb and 30 Mar 2003 for IOP4.

Observation ID	Easting (m)	Northing (m)	IOP 3 observed SWE (cm)	IOP 3 difference SWE (cm)	IOP 4 observed SWE (cm)	IOP 4 difference SWE (cm)
Buffalo Pass ISA	357 576	4 488 391	71.2	0.8	109.8	−24.8
Spring Creek ISA	351 058	4 487 951	51.9	1.7	67.2	−4.1
Walton Creek ISA	360 145	4 473 579	50.4	−0.7	66.9	−6.6
301	—	—	—	—	—	—
302	—	—	—	—	—	—
303	345 190	4 470 221	—	—	16.3	−0.7
304	344 533	4 472 145	—	—	16.5	3.4
305	346 238	4 472 443	—	—	17.5	−4.9
306	353 939	4 467 181	—	—	32.0	7.5
307	—	—	—	—	—	—
308	353 755	4 485 596	—	—	34.0	28.5
309	351 275	4 490 443	—	—	30.5	19.0
310	362 298	4 488 299	—	—	32.5	28.9
311	366 324	4 488 870	—	—	21.8	38.0
312	354 381	4 475 079	—	—	27.7	23.7
313	361 927	4 470 916	—	—	51.3	−1.8
314	—	—	—	—	—	—
315	—	—	—	—	—	—
316	—	—	—	—	—	—
317	368 808	4 477 388	—	—	31.0	12.4
318	—	—	—	—	—	—
319	366 424	4 477 397	—	—	32.0	15.6
320	—	—	—	—	—	—
321	—	—	—	—	—	—
322	—	—	—	—	—	—

treeline), and patterns associated with the vegetation distribution. Intuitively, the general distribution patterns simulated by the model (Fig. 5c) are considerably more realistic than those defined by observations alone (Fig. 5a).

Using the observations defined in Fig. 2a, the average modeled SWE (Fig. 5c) corresponding to each ISA and GAMMA flight line was calculated. Figure 8a compares the modeled and observed SWE for each Fraser observation area. Differences between the simulated and observed values (modeled minus observed; Table 2) were then interpolated across the simulation domain using the Barnes scheme (Fig. 5d). The largest difference occurred in the south-southeast area of the domain and is heavily leveraged by GAMMA flight line 115 SWE values. This flight line traverses an alpine ridge that, in the natural and modeled systems, is characterized by alternating large snow erosion areas and deep snowdrifts located within a few meters of each other [see Elder et al. (1991) and Sturm et al. (2001) for descriptions of this phenomenon]. Thus, small deviations in GAMMA flight positioning have important consequences for measured SWE. Unfortunately, we do not have enough ground-based observations to quantify these potential errors. In addition, the GAMMA system saturates under conditions of very deep snow, and SWE variations over a flight line also produce SWE underestimates (Cork and Loijens 1980; Carroll and Carroll 1989a). Thus, GAMMA SWE is potentially underestimated under flight line 115.

The North Park MSA simulation results for IOP3 are presented in Fig. 6. The IOP4 SWE distributions are close to zero (Table 1). The Barnes-interpolated ISA and GAMMA SWE observations (Fig. 6a) display a relatively uniform distribution, with higher values in the northern and eastern parts of the domain. The SWE values are considerably lower than the Fraser MSA. To improve clarity, the ISA and GAMMA observation masks were omitted in Fig. 6.

The North Park precipitation correction factor distributions had a general east–west gradient (Fig. 6b). As with the Fraser simulation, the model-generated North Park IOP3 SWE distribution (Fig. 6c) shows much more spatial structure than existing observations (Fig. 6a). Again, the general distribution patterns simulated by the model are intuitively more realistic than those defined by the observations. Using the observations defined in Fig. 3a, the average modeled SWE (Fig. 6c)

TABLE 5. Meteorological data sites and variables used in the model simulations (Fig. 1b).

Site description	Station ID	Easting (m)	Northing (m)	Elevation (m)	Variables*
Fraser MSA					
Alpine-CLPX	1101	426 340	4 411 238	3598	*T, R, W, D*
Fool Creek-CLPX	1102	425 791	4 414 910	3101	*T, R*
Headquarters-CLPX	1103	424 440	4 417 564	2767	*T, R*
St. Louis Creek-CLPX	1104	425 729	4 419 936	2725	*T, R*
Lower sublimation-FRASER**	1105	422 413	4 416 131	2974	*T, R*
Upper sublimation-FRASER	1106	420 154	4 415 932	3222	*T, R*
Bottle Ridge-FRASER	1107	419 664	4 416 526	3371	*T, R, W, D*
Clearcut-FRASER	1108	423 581	4 416 575	2853	*T, R*
Forest-FRASER	1109	423 633	4 416 696	2860	*T, R*
Arrow-SNOTEL	1110	435 902	4 418 814	2950	*T*
Berthoud Summit-SNOTEL	1111	434 338	4 405 841	3450	*T*
Jones Pass-SNOTEL	1112	422 915	4 402 284	3170	*T*
Middle Fork Camp-SNOTEL	1113	411 566	4 406 070	2743	*T*
25 LAPS points	1151–1175	—	—	—	*T, R, W, D, P*
North Park MSA					
Illinois River-CLPX	2201	394 004	4 505 710	2472	*T, R, W, D*
Michigan River-CLPX	2202	400 146	4 500 029	2596	*T, R, W, D*
Potter Creek-CLPX	2203	388 157	4 502 717	2478	*T, R, W, D*
Roach-SNOTEL	2204	404 377	4 513 510	3002	*T*
Flux Tower-CLPX	2205	388 085	4 501 734	2477	*T, R, W, D*
25 LAPS points	2251–2275	—	—	—	*T, R, W, D, P*
Rabbit Ears MSA					
Buffalo Pass-CLPX	3301	357 887	4 488 407	3233	*T, R, W, D*
Spring Creek-CLPX	3302	351 126	4 487 974	2804	*T, R, W, D*
Walton Creek-CLPX	3303	360 335	4 473 447	2950	*T, R, W, D*
Columbine-SNOTEL	3304	362 779	4 473 410	2794	*T*
Dry Lake-SNOTEL	3305	348 990	4 488 445	2515	*T*
Rabbit Ears-SNOTEL	3306	352 863	4 469 933	2911	*T*
Tower-SNOTEL	3307	358 815	4 488 253	3219	*T*
Dry Lake-RAWS	3308	348 990	4 488 445	2515	*T, R*
Storm Peak-DRI	3309	352 450	4 479 159	3210	*T, R, W, D*
25 LAPS points	3351–3375	—	—	—	*T, R, W, D, P*

* Meteorological variables available at each site: T = air temperature, R = relative humidity, W = wind speed, D = wind direction, and P = precipitation.

** FRASER = Fraser Experimental Forest.

corresponding to each ISA and GAMMA flight line was calculated. Figure 8b compares the modeled and observed SWE for each North Park observation area. The differences between the simulated and observed values (modeled minus observed; Table 3) were then interpolated across the simulation domain using the Barnes scheme (Fig. 6d).

Rabbit Ears MSA simulation results for IOP4 are presented in Fig. 7. The Barnes-interpolated ISA and GAMMA SWE observations (Fig. 7a) include a north–south band of higher values through the center of the domain, with relatively lower values to the east and west. The highest SWE values in this center band are located in the northern part of the domain. For reference, the Rabbit Ears, IOP4, and ISA and GAMMA observation areas are included in Fig. 7.

The Rabbit Ears precipitation correction factor distributions mimicked observed SWE distributions (Fig.

7b). These essentially provided different corrections for the eastern area, central highlands, and western valleys of the simulation domain. As with the Fraser simulation, the model-generated Rabbit Ears IOP4 SWE distribution (Fig. 7c) shows much more spatial structure than the observations. And, similar to the North Park simulation, the Rabbit Ears simulation (Fig. 7c) generally reproduced the regional pattern found in the observations (Fig. 7a). Again, the general distribution patterns simulated by the model are intuitively more realistic than those defined by the observations.

Using the observation mask defined in Fig. 4a, the average modeled SWE (Fig. 7c) corresponding to each ISA and GAMMA flight line was calculated. Figure 8c compares the modeled and observed SWE for each Rabbit Ears observation area. The differences between the simulated and observed SWE (modeled minus observed; Table 4) were interpolated across the simula-
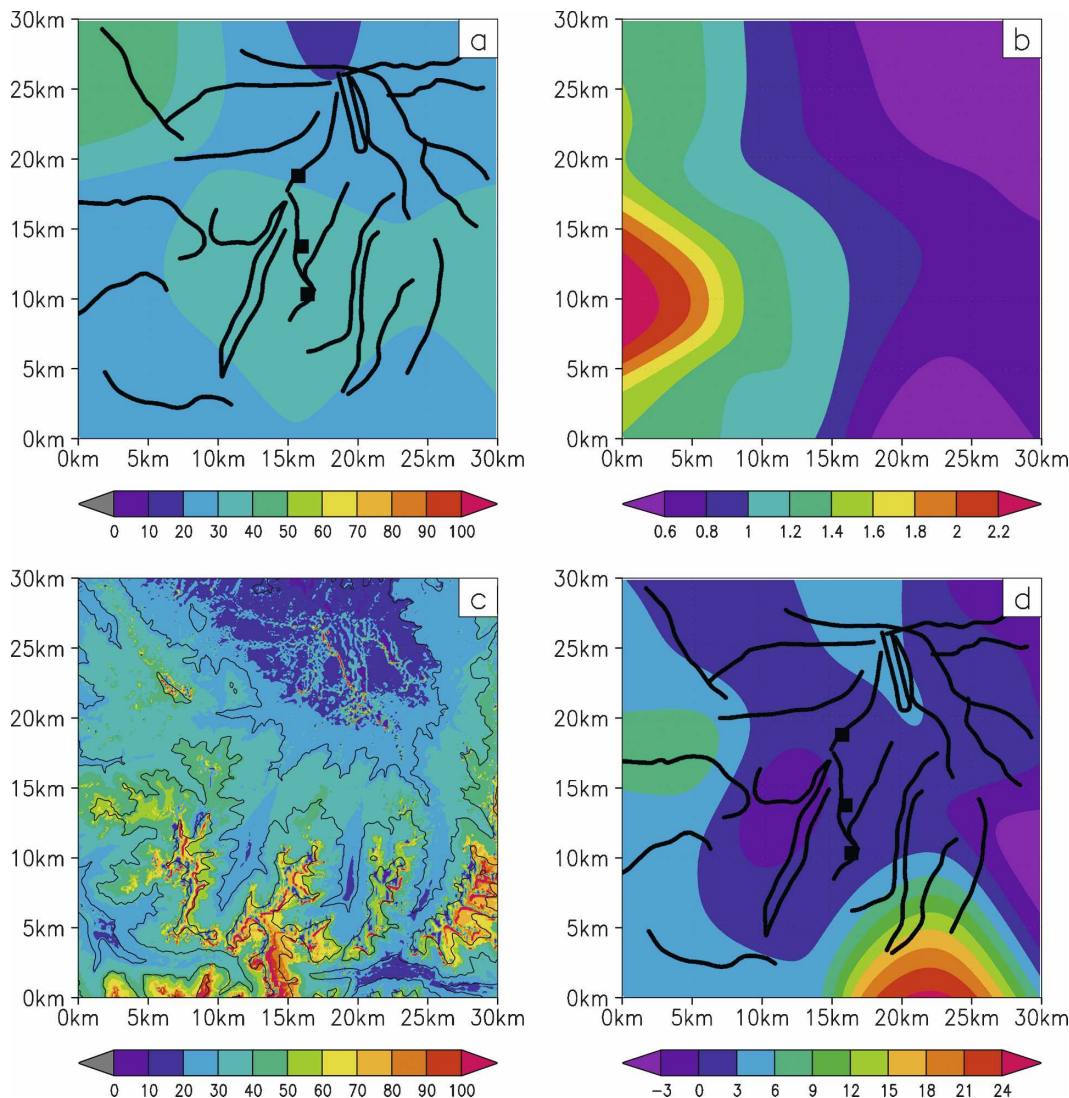
FIG. 5. The Fraser MSA on 25 Mar 2003 during IOP4. (a) ISA and GAMMA SWE (cm) observations gridded to the simulation domain. Also shown in black are the ISA (squares) and GAMMA (lines) observation masks. (b) The average of the two data assimilation precipitation correction factor (nondimensional) distributions (IOP3 and IOP4) used in the simulations. (c) Model-simulated SWE (cm; black lines are topographic contours). (d) SWE differences (cm; modeled − observed) calculated over the ISAs and GAMMA flight lines and interpolated over the simulation domain, and the ISA and GAMMA observation masks.

tion domain using the Barnes scheme (Fig. 7d). The largest difference occurred in the northeast area of the domain and is influenced by SWE values associated with GAMMA line 311. The model simulation (Fig. 7c) included several deep drifts in the northeast corner that were underneath flight line 311. This yielded corresponding modeled SWE values that were nearly 3 times greater than the GAMMA observations (Table 4). Either the model overestimates snowdrift SWE, and/or the GAMMA system underestimates SWE in very deep drifts because the system saturates [e.g., Carroll and Carroll (1989b) used GAMMA to measure 60-cm SWE

in forests, with errors of approximately 12%; other NOHRSC efforts indicate any gamma radiation emitted through more than 70–90 cm SWE is minimal (T. R. Carroll and D. W. Cline 2007, personal communication)].

Model simulations produce the full accumulation season over each of the MSA domains. As an example, the midmonth time evolution of Fraser MSA SWE is provided in Fig. 9. In this area, there were two main accumulation periods: early winter (October–November) and late winter (February–March), with little accumulation occurring in January–February.
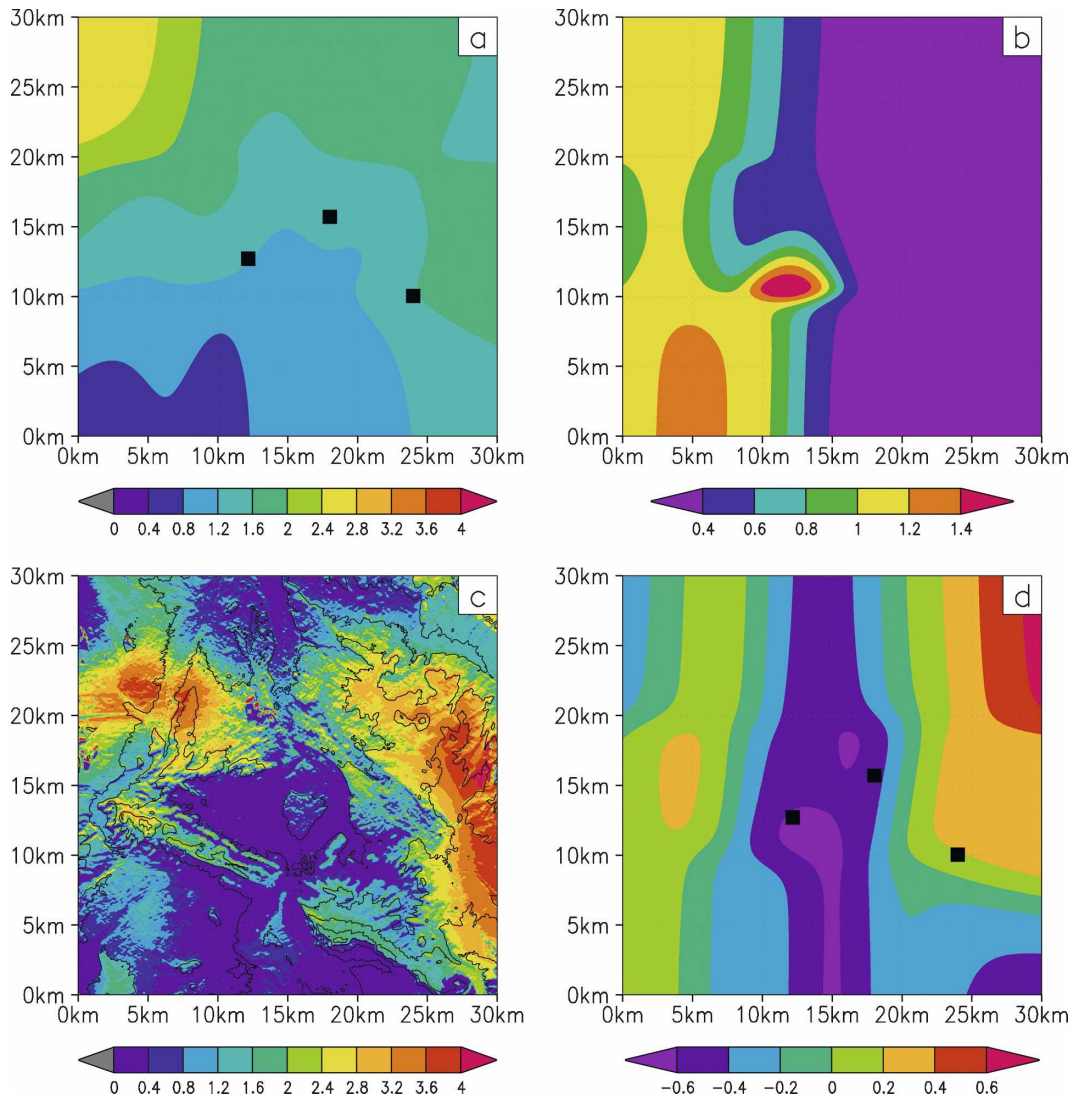
FIG. 6. Same as Fig. 5, but for the North Park MSA on 21 Feb 2003 during IOP3. To improve clarity, the GAMMA observation masks were omitted from (a) and (d).

5. Discussion

The modeling system and associated model simulations represent a combined approach in which the MicroMet and SnowModel physics defines the spatial SWE *patterns* and observations and the associated SnowAssim reconcile SWE *magnitudes*. Naturally, the quality of the output depends on the limitations of the modeling system and input datasets. Because general model limitations have been recently discussed elsewhere (Liston and Elder 2006a, 2006b; Liston and Hiemstra 2008; Liston et al. 2007), here we present additional details of the observational datasets relevant to these simulations.

ISA-specific ground-based snow depth and density measurements and MSA-wide airborne GAMMA SWE measurements were used in the simulations. The ISA measurements included numerous snow depth observations within each 1-km^2 ISA (Elder et al. 2008a). Thus, sub-ISA snow distribution information was available for use in the model simulations. Because of this paper's focus on describing coarser-scale MSA-level SWE gradients and distributions as well as scale-appropriate terrain and vegetation data, we chose to use ISA-average observations to define scale-appropriate regional SWE variations. At finer scales, specific terrain and vegetation features as well as observational locations play a larger role in comparing observed and modeled SWE values (Hiemstra et al. 2006a).
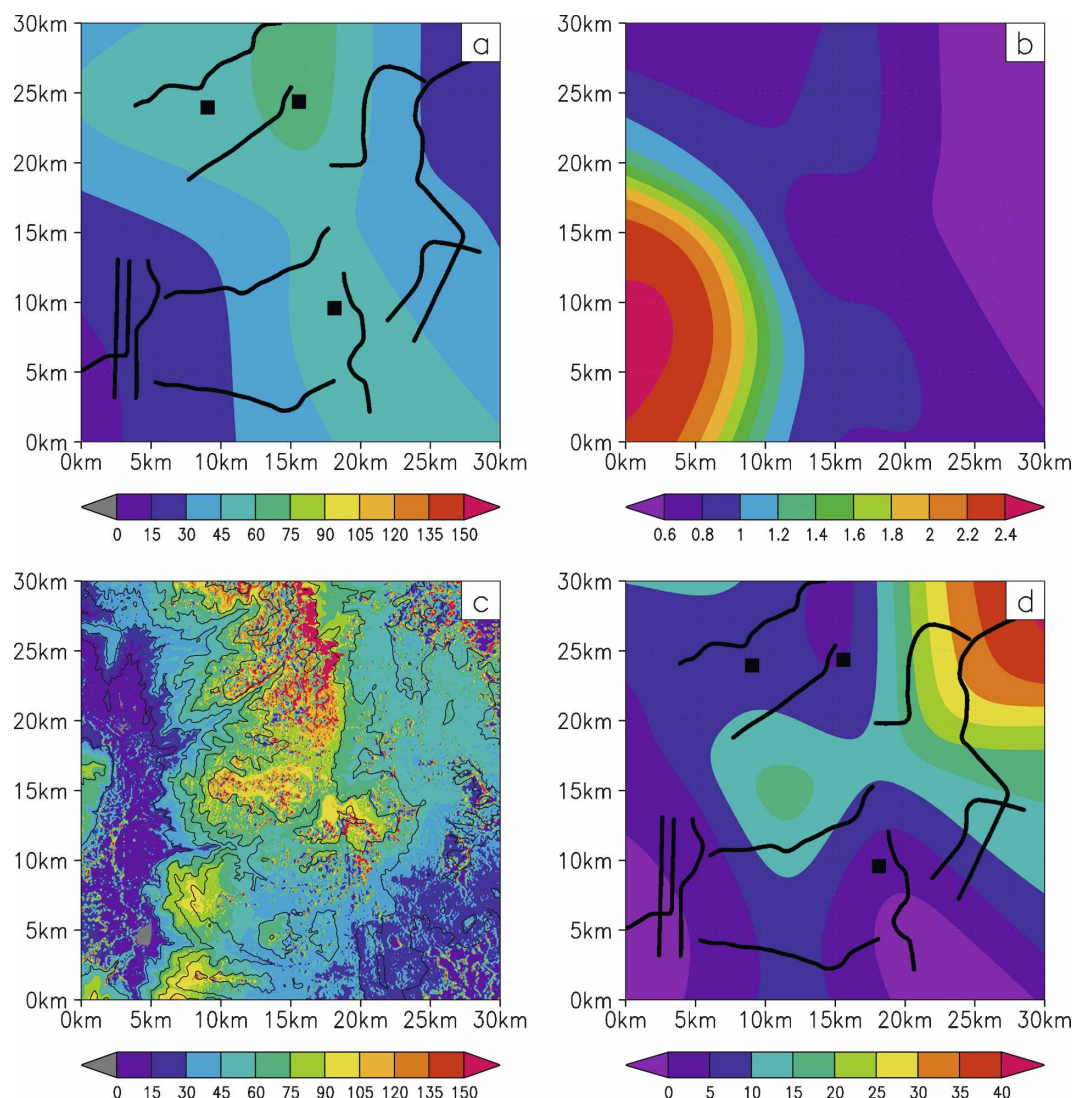
FIG. 7. Same as Fig. 5, but for the Rabbit Ears MSA on 30 Mar 2003 during IOP4.

Model simulations incorporated GAMMA observations in a similar fashion to ISA observations to capture regional SWE variations, whereas SnowModel defined the finer details. These GAMMA data provide an integrated (average) SWE over flight line areas covering approximately 10 km × 300 m. For the Fraser (Fig. 2) and Rabbit Ears (Fig. 4) MSAs, individual flight lines span considerable topographic gradients, which are likely associated with a wide range in SWE. In addition, for these two cases, flight lines possess a considerable bias toward lines following streams. Although this was done largely for flight crew safety, the lack of ridge and cross-valley observations imposes biases in the model outputs.

Comparison of the ISA and GAMMA observations listed in Tables 2 and 4 raise questions regarding the appropriateness of assimilating the block-corrected GAMMA observations for the Rabbit Ears case. The Fraser ISA and GAMMA data values (Table 2) are equivalent and, in general, the topography and vegetation represented by the ISAs are similar to the GAMMA lines. In contrast, there are distinct differences in the Rabbit Ears (Table 4) data. For Rabbit Ears, the ISA observations are approximately 2–3 times greater than the GAMMA measurements. We believe it is reasonable that the Buffalo Pass and Walton Creek ISAs are greater than any of the GAMMA lines; there are no full GAMMA lines at elevations similar to these ISAs, and these ISAs routinely possess some of the deepest snow in Colorado (Doesken and Judson 1996). Although the Spring Creek ISA is roughly at the same average elevation of GAMMA lines 306, 308, 309, and
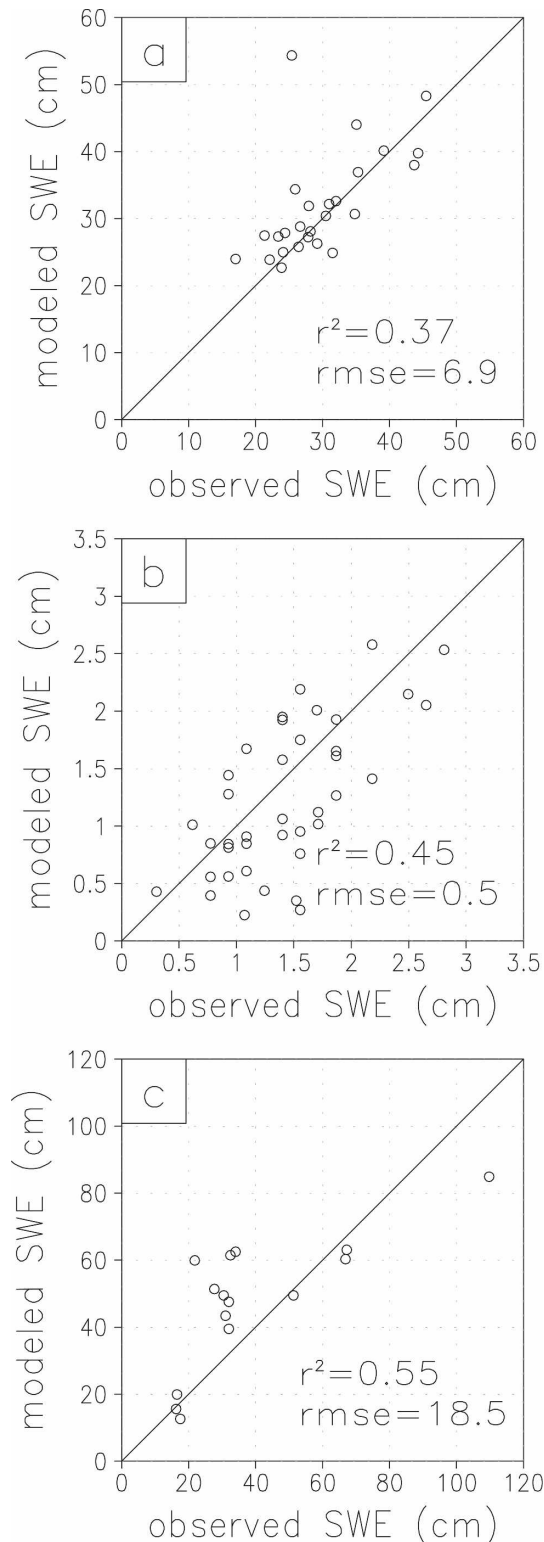
FIG. 8. Comparison of modeled and observed SWE over the ISA and GAMMA observation masks for (a) IOP4, Fraser; (b) IOP3, North Park; and (c) IOP4, Rabbit Ears MSAs. Panels (a)–(c) correspond to Figs. 5d–7d, respectively. Included are the square of the linear correlation coefficient r^2 and rmse.

312, and the general aspect of these lines and the ISA are also similar, these flight lines extend from the deeper SWE areas at elevations above Spring Creek ISA to the shallow SWE areas in the lowlands below (Fig. 4). Spring Creek in situ observations had roughly 2 times more SWE than these GAMMA lines. Even if the GAMMA observations in this area are error free, they may not be representative of the ISAs where in situ observations were collected, or of the mean MSA conditions. Unfortunately, we have no way to quantify this possible error.

As part of these simulations, we ran the model only during the winter accumulation season. Part of our reasoning for not including the spring ablation period was the lack of snow observations. It is certainly possible to run the model during that time, but it would do so unconstrained by observations and possibly contain unacceptable errors. As part of a forthcoming simulation effort, we anticipate using melt-period sonic sounder and reflected-radiation observations from the meteorological stations, as well as various remote sensing datasets, to constrain the model during snowmelt. To satisfy computational constraints, model simulations during the accumulation period were performed using a one-day time step. As part of the model simulations during the spring and early summer ablation periods, the simulations must resolve the diurnal cycle (e.g., for temperature and incoming solar radiation) to realistically reproduce snow cover depletion. The ablation-period observations and higher temporal resolution simulations would be used as part of other data assimilation model runs that would complete the full annual snow cycle for each of the CLPX MSAs.

As with any snow-evolution simulations, a significant challenge to the modeling effort is to define appropriate precipitation forcing for the model runs. We chose to use LAPS precipitation fields as our starting point, under the assumption that they provided a consistent dataset covering each MSA simulation domain. In reality, because the data assimilated as part of the LAPS analyses are not the same across each of the MSAs (e.g., the radar-defined precipitation fields originating in Denver, Colorado, did not reach the Rabbit Ears MSA), the precipitation data used required different corrections for each MSA. Alternative precipitation datasets that could have been used to drive the simulations include those available from the snowpack telemetry (SNOTEL) and other meteorological stations listed in Table 5. Unfortunately, most of these did not measure winter precipitation, and the ones that did have their own deficiencies and limitations that require correction before use (Yang et al. 1998, 2005; Liston and Sturm 2004).
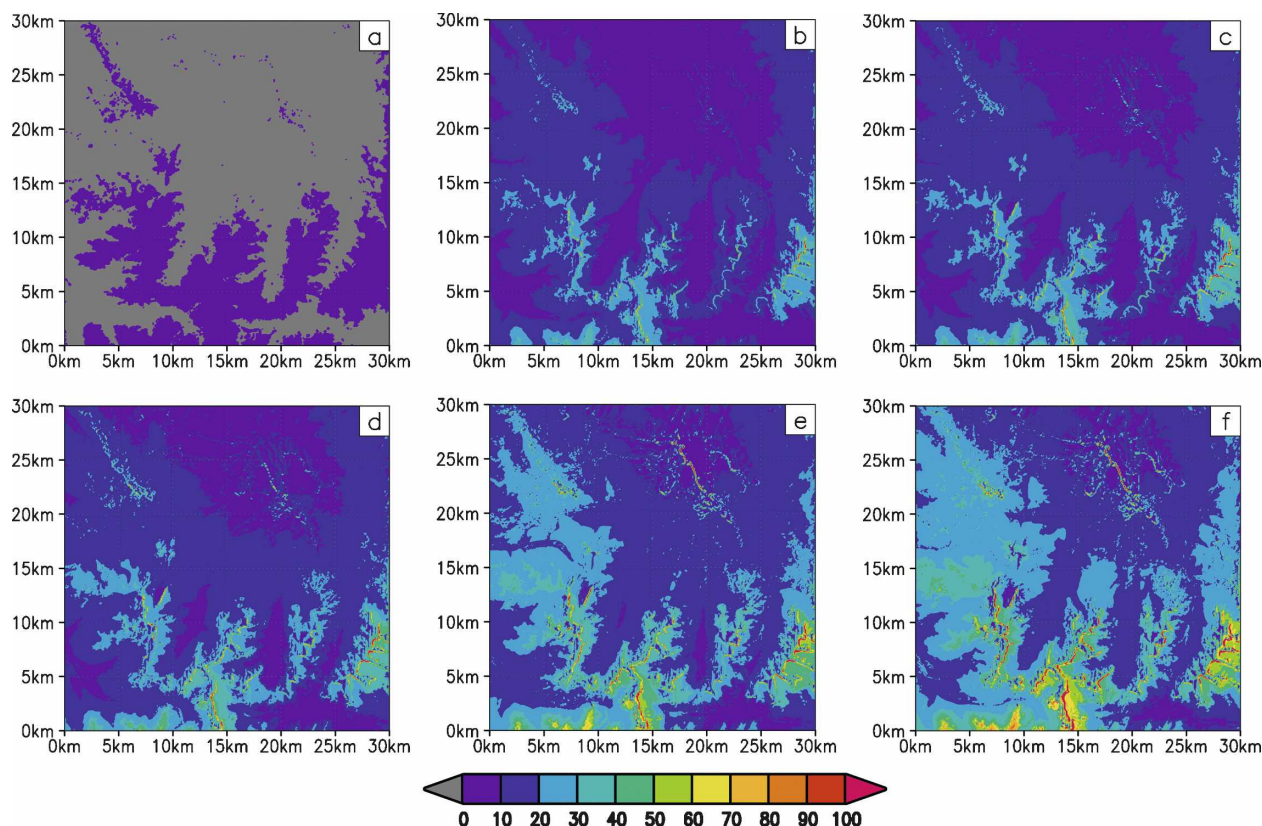
FIG. 9. Model-simulated, monthly SWE (cm) time evolution for Fraser MSA. (a) 15 Oct 2002, (b) 15 Nov 2002, (c) 15 Dec 2002, (d) 15 Jan 2003, (e) 15 Feb 2003, and (f) 15 Mar 2003.

6. Conclusions

As part of the NASA CLPX project, we recognized the need to unite disparate snow-related tools and datasets into one coherent package. Simulating realistic, high-resolution snow distributions require a snow-evolution modeling system that includes the ability to distribute available meteorological forcing, simulate snowpack accumulation and ablation processes, and assimilate snow-related observations. Available tools that needed to be developed and merged for this system included a high-resolution meteorological model; a snow model capable of accounting for snow-forest interactions, blowing and drifting snow, snow-property evolution, and snowmelt; and a data assimilation model capable of pushing model simulations toward snow observations. Available snow-related observations included ground-based measurements, airborne-based observations, and satellite-based remote sensing datasets. Additional supporting datasets available for use included high-resolution (e.g., 30 m) topography and vegetation distributions. To accomplish our CLPX goals, we developed and merged a collection of three models: MicroMet, SnowModel, and SnowAssim. Mi-

croMet provided the meteorological distributions required to drive SnowModel. SnowModel was used to evolve the distributed snowpack and its associate snow properties; it is made up of three submodels: EnBal calculates surface energy exchanges, SnowPack simulates snow depth and water-equivalent evolution, and SnowTran-3D accounts for snow redistribution by wind. SnowModel was coupled to SnowAssim, which adjusted simulated SWE distributions toward available ground-based and remotely sensed SWE observations.

The combined MicroMet–SnowModel–SnowAssim modeling system was used to create SWE distributions for three 30 km × 30 km study areas in north-central Colorado as part of the CLPX program. The modeled distributions included snow-forest interactions, wind-transported snow, and the orographic influence on atmospheric forcing variables such as temperature and precipitation. The simulated SWE distributions were characterized by high-resolution (30 m and greater) spatial distributions governed by the combined interactions among wind, snow, and vegetation. Areas without trees included drifts formed by wind redistribution of snow. The forested areas had relatively uniform snow distributions, which displayed the influences of tem-

perature and precipitation and their interactions with local and regional topography. The simulated snow distributions were much more complex and spatially variable than the distributions created using the observed SWE alone. In fact, generating spatial distributions using just the observations generally created physically unrealistic snow distributions.

The resulting datasets represent our best estimate of snow distributions in the complex landscapes of north-central Colorado. They provide examples of subgrid snow distributions for coarse-scale atmospheric and terrestrial modeling applications, for defining subgrid snow distributions in remote sensing products such as the 25 km × 25 km AMSR-E SWE datasets, and for water resource applications concerned with spring snowmelt runoff. The methodologies presented could also be applied to other cold regions and cold season landscapes to help understand snow-distribution characteristics and features in those areas.

REFERENCES

Albers, S. C., 1995: The LAPS wind analysis. *Wea. Forecasting,* **10,** 342–352.

——, J. A. McGinley, D. L. Birkenheuer, and J. R. Smart, 1996: The Local Analysis and Prediction System (LAPS): Analyses of clouds, precipitation, and temperature. *Wea. Forecasting,* **11,** 273–287.

Balk, B., and K. Elder, 2000: Combining binary decision tree and geostatistical methods to estimate snow distribution in a mountain watershed. *Water Resour. Res.,* **36,** 13–26.

Barnes, S. L., 1964: A technique for maximizing details in numerical weather map analysis. *J. Appl. Meteor.,* **3,** 396–409.

——, 1973: Mesoscale objective analysis using weighted time-series observations. NOAA Tech. Memo. ERL NSSL-62, National Severe Storms Laboratory, Norman, OK 73069, 60 pp. [NTIS COM-73-10781].

Benedict, J. B., 1993: Influence of snow upon rates of granodiorite weathering, Colorado Front Range, USA. *Boreas,* **22,** 87–92.

Billings, W. D., 1973: Arctic and alpine vegetations: Similarities, differences, and susceptibility to disturbance. *BioScience,* **23,** 697–704.

——, and L. C. Bliss, 1959: An alpine snowbank environment and its effects on vegetation, plant development, and productivity. *Ecology,* **40,** 388–397.

Birkenheuer, D., 1999: The effect of using digital satellite imagery in the LAPS moisture analysis. *Wea. Forecasting,* **14,** 782–788.

Blöschl, G., 1999: Scaling issues in snow hydrology. *Hydrol. Processes,* **13,** 2149–2175.

Brooks, P. D., D. M. McKnight, and K. E. Bencala, 1999: The relationship between soil heterotrophic activity, soil dissolved organic carbon (DOC) leachate, and catchment-scale DOC export in headwater catchments. *Water Resour. Res.,* **35,** 1895–1902.

Carroll, S. S., and T. R. Carroll, 1989a: Effect of uneven snow cover on airborne snow water equivalent estimates obtained by measuring terrestrial gamma radiation. *Water Resour. Res.,* **25,** 1505–1510.

——, and ——, 1989b: Effect of forest biomass on airborne snow water equivalent estimates obtained by measuring terrestrial gamma radiation. *Remote Sens. Environ.,* **27,** 313–319.

Carroll, T. R., 1987: Operational airborne measurements of snow water equivalent and soil moisture using terrestrial gamma radiation in the United States. *Proc. Large Scale Effects of Seasonal Snow Cover Symp.,* Vancouver, BC, Canada, IAHS Publication 166, 213–223.

Cline, D., and Coauthors, 2008: NASA Cold Land Processes Experiment (CLPX 2002/03): Airborne remote sensing. *J. Hydrometeor.,* in press.

Cohen, J., and D. Entekhabi, 2001: The influence of snow cover on Northern Hemisphere climate variability. *Atmos.–Ocean,* **39,** 35–53.

Cork, H. F., and H. S. Loijens, 1980: The effect of snow drifting on gamma snow survey results. *J. Hydrol.,* **48,** 41–51.

Doesken, N. J., and A. Judson, 1996: *The Snow Booklet: A Guide to the Science, Climatology, and Measurement of Snow in the United States.* Department of Atmospheric Science, Colorado State University, 84 pp.

Elder, K., J. Dozier, and J. Michaelsen, 1991: Snow accumulation and distribution in an alpine watershed. *Water Resour. Res.,* **27,** 1541–1552.

——, D. Cline, G. E. Liston, and R. Armstrong, 2008a: NASA Cold Land Processes Experiment (CLPX 2002/03): Field measurements of snowpack properties and soil moisture. *J. Hydrometeor.,* in press.

——, ——, G. Goodbody, P. Houser, G. E. Liston, L. Mahrt, and N. Rutter, 2008b: NASA Cold Land Processes Experiment (CLPX 2002/03): Ground-based and near-surface meteorological observations. *J. Hydrometeor.,* in press.

Ellis, A. W., and D. J. Leathers, 1999: Analysis of cold airmass temperature modification across the U.S. Great Plains as a consequence of snow depth and albedo. *J. Appl. Meteor.,* **38,** 696–711.

Essery, R., and J. Pomeroy, 2004: Vegetation and topographic control of wind-blown snow distributions in distributed and aggregated simulations for an arctic tundra basin. *J. Hydrometeor.,* **5,** 735–744.

Fagre, D. B., D. L. Peterson, and A. E. Hessl, 2003: Taking the pulse of mountains: Ecosystem responses to climatic variability. *Climatic Change,* **59,** 263–282.

Gelfan, A. N., J. W. Pomeroy, and L. S. Kuchment, 2004: Modeling forest cover influences on snow accumulation, sublimation, and melt. *J. Hydrometeor.,* **5,** 785–803.

Hiemstra, C. A., G. E. Liston, and W. A. Reiners, 2006a: Observing, modelling, and validating snow redistribution by wind in a Wyoming upper treeline landscape. *Ecol. Modell.,* **197,** 35–51.

——, ——, R. A. Pielke Sr., D. L. Birkenheuer, and S. C. Albers, 2006b: Comparing Local Analysis and Prediction System (LAPS) assimilations with independent observations. *Wea. Forecasting,* **21,** 1024–1040.

Hinzman, L. D., D. L. Kane, C. S. Benson, and K. R. Everett, 1996: Energy balance and hydrological processes in an Arctic watershed. *Landscape Function: Implications for Ecosystem Response to Disturbance. A Case Study in Arctic Tundra,* J. F.

Reynolds and J. D. Tenhunen, Eds., Ecological Studies Series, Vol. 120, Springer-Verlag, 131–154.

——, D. J. Goering, and D. L. Kane, 1998: A distributed thermal model for calculating soil temperature profiles and depth of thaw in permafrost regions. *J. Geophys. Res.,* **103** (D22), 28 975–28 991.

Jones, W., and T. R. Carroll, 1983: Error analysis of airborne gamma radiation soil moisture measurements. *Agric. For. Meteor.,* **28,** 19–30.

Kane, D. L., L. D. Hinzman, C. S. Benson, and G. E. Liston, 1991: Snow hydrology of a headwater Arctic basin. 1. Physical measurements and process studies. *Water Resour. Res.,* **27,** 1099–1109.

Koch, S. E., M. DesJardins, and P. J. Kocin, 1983: An interactive Barnes objective map analysis scheme for use with satellite and conventional data. *J. Climate Appl. Meteor.,* **22,** 1487–1503.

Liston, G. E., 1995: Local advection of momentum, heat, and moisture during the melt of patchy snow covers. *J. Appl. Meteor.,* **34,** 1705–1715.

——, 2004: Representing subgrid snow cover heterogeneities in regional and global models. *J. Climate,* **17,** 1381–1397.

——, and D. K. Hall, 1995: An energy balance model of lake ice evolution. *J. Glaciol.,* **41,** 373–382.

——, and M. Sturm, 1998: A snow-transport model for complex terrain. *J. Glaciol.,* **44,** 498–516.

——, and ——, 2002: Winter precipitation patterns in arctic Alaska determined from a blowing-snow model and snow-depth observations. *J. Hydrometeor.,* **3,** 646–659.

——, and ——, 2004: The role of winter sublimation in the Arctic moisture budget. *Nord. Hydrol.,* **35,** 325–334.

——, and K. Elder, 2006a: A distributed snow-evolution modeling system (SnowModel). *J. Hydrometeor.,* **7,** 1259–1276.

——, and ——, 2006b: A meteorological distribution system for high-resolution terrestrial modeling (MicroMet). *J. Hydrometeor.,* **7,** 217–234.

——, and C. A. Hiemstra, 2008: A simple data assimilation system for complex snow distributions (SnowAssim). *J. Hydrometeor.,* **9,** 989–1004.

——, J.-G. Winther, O. Bruland, H. Elvehøy, K. Sand, and L. Karlöf, 2000: Snow and blue-ice distribution patterns on the coastal Antarctic ice sheet. *Antarct. Sci.,* **12,** 69–79.

——, J. P. McFadden, M. Sturm, and R. A. Pielke Sr., 2002: Modelled changes in arctic tundra snow, energy and moisture fluxes due to increased shrubs. *Global Change Biol.,* **8,** 17–32.

——, R. B. Haehnel, M. Sturm, C. A. Hiemstra, S. Berezovskaya, and R. D. Tabler, 2007: Simulating complex snow distributions in windy environments using SnowTran-3D. *J. Glaciol.,* **53,** 241–256.

——, D. L. Birkenheuer, C. A. Hiemstra, D. Cline, and K. Elder, 2008: NASA Cold Land Processes Experiment (CLPX 2002/03): Atmospheric analyses datasets. *J. Hydrometeor.,* **9,** 952–956.

Luce, C. H., D. G. Tarboton, and K. R. Cooley, 1998: The influence of the spatial distribution of snow on basin-averaged snowmelt. *Hydrol. Processes,* **12,** 1671–1683.

Marsh, P., 1999: Snowcover formation and melt: Recent advances and future prospects. *Hydrol. Processes,* **13,** 2117–2134.

McGinley, J. A., S. C. Albers, and P. A. Stamus, 1991: Validation of a composite convective index as defined by a real-time local analysis system. *Wea. Forecasting,* **6,** 337–356.

Meek, D. W., and J. L. Hatfield, 1994: Data quality checking for single station meteorological variables. *Agric. For. Meteor.,* **69,** 85–109.

Nelson, F. E., K. M. Hinkel, N. I. Shiklomanov, G. R. Mueller, L. L. Miller, and D. A. Walker, 1998: Active-layer thickness in north central Alaska: Systematic sampling, scale, and spatial autocorrelation. *J. Geophys. Res.,* **103** (D22), 28 963–28 973.

Peck, E., T. R. Carroll, and S. Vandermark, 1980: Operational aerial snow surveying in the United States. *Hydrol. Sci. Bull.,* **25,** 51–62.

Pomeroy, J. W., B. Toth, R. J. Granger, N. R. Hedstrom, and R. L. H. Essery, 2003: Variation in surface energetics during snowmelt in a subarctic mountain catchment. *J. Hydrometeor.,* **4,** 702–719.

Robinson, D. A., K. F. Dewey, and R. R. Heim Jr., 1993: Global snow cover monitoring: An update. *Bull. Amer. Meteor. Soc.,* **74,** 1689–1696.

Seastedt, T. R., 2001: Soils. *Structure and Function of an Alpine Ecosystem: Niwot Ridge, Colorado,* W. D. Bowman and T. R. Seastedt, Eds., Oxford University Press, 157–173.

Serreze, M. C., M. P. Clark, R. L. Armstrong, D. A. McGinnis, and R. S. Pulwarty, 1999: Characteristics of the western United States snowpack from snowpack telemetry (SNOTEL) data. *Water Resour. Res.,* **35,** 2145–2160.

Sturm, M., J. Holmgren, and G. E. Liston, 1995: A seasonal snow cover classification system for local to global applications. *J. Climate,* **8,** 1261–1283.

——, J. P. McFadden, G. E. Liston, F. S. Chapin III, C. H. Racine, and J. Holmgren, 2001: Snow–shrub interactions in arctic tundra: A hypothesis with climatic implications. *J. Climate,* **14,** 336–344.

Taras, B., M. Sturm, and G. E. Liston, 2002: Snow–ground interface temperatures in the Kuparuk River Basin, arctic Alaska: Measurements and model. *J. Hydrometeor.,* **3,** 377–394.

Vogelmann, J. E., S. M. Howard, L. M. Yang, C. R. Larson, B. K. Wylie, and N. Van Driel, 2001: Completion of the 1990s National Land Cover Data set for the conterminous United States from Landsat Thematic Mapper data and ancillary data sources. *Photogramm. Eng. Remote Sens.,* **67,** 650–652.

Wahl, K. L., 1992: Evaluation of trends in runoff in the western United States. *Managing Water Resources during Global Change,* R. Herrmann, Ed., American Water Resources Association, 701–710.

Williams, M. W., M. V. Losleben, and H. B. Hamann, 2002: Alpine areas in the Colorado Front Range as monitors of climate change and ecosystem response. *Geogr. Rev.,* **92,** 180–191.

Yang, D., B. E. Goodison, J. R. Metcalfe, V. S. Golubev, R. Bates, T. Pangburn, and C. L. Hanson, 1998: Accuracy of NWS 8″ standard nonrecording precipitation gauge: Results and application of WMO intercomparison. *J. Atmos. Oceanic Technol.,* **15,** 54–68.

——, D. Kane, Z. Zhang, D. Legates, and B. Goodison, 2005: Bias corrections of long-term (1973–2004) daily precipitation data over the northern regions. *Geophys. Res. Lett.,* **32,** L19501, doi:10.1029/2005GL024057.

Zhang, T., R. L. Armstrong, and J. Smith, 2003: Investigation of the near-surface soil freeze-thaw cycle in the contiguous United States: Algorithm development and validation. *J. Geophys. Res.,* **108** (D22), 8860, doi:10.1029/2003JD003530.